Photoactivatable Xanthone (PaX) Dyes Enable Quantitative, Dual Color, and Live-Cell MINFLUX Nanoscopy

Michael Remmel, Jessica Matthias, Richard Lincoln, Jan Keller-Findeisen, Alexey N. Butkevich, Mariano L. Bossi, and Stefan W. Hell*

The single-molecule localization concept MINFLUX has triggered a reevaluation of the features of fluorophores for attaining nanometer-scale resolution. MINFLUX nanoscopy benefits from temporally controlled fluorescence ("on"/"off") photoswitching. Combined with an irreversible switching behavior, the localization process is expected to turn highly efficient and quantitative data analysis simple. The potential in the recently reported photoactivable xanthone (PaX) dyes is recognized to extend the list of molecular switches used for MINFLUX with 561 nm excitation beyond the fluorescent protein mMaple. The MINFLUX localization success rates of PaX_{560}, $PaX+_{560}$, and mMaple are quantitatively compared by analyzing the effective labeling efficiency of endogenously tagged nuclear pore complexes. The PaX dyes prove to be superior to mMaple and on par with the best reversible molecular switches routinely used in single-molecule localization microscopy. Moreover, the rationally designed PaX_{595} is introduced for complementing PaX_{560} in dual color 561 nm MINFLUX imaging based on spectral classification and the deterministic, irreversible, and additive-independent nature of PaX photoactivation is showcased in fast live-cell MINFLUX imaging. The PaX dyes meet the demands of MINFLUX for a robust readout of each label position and fill the void of reliable fluorophores dedicated to 561 nm MINFLUX imaging.

M. Remmel, J. Matthias[+], R. Lincoln, A. N. Butkevich, M. L. Bossi,
S. W. Hell
Department of Optical Nanoscopy
Max Planck Institute for Medical Research
69120 Heidelberg, Germany
E-mail: Stefan.Hell@mpinat.mpg.de
J. Keller-Findeisen[++], A. N. Butkevich, M. L. Bossi, S. W. Hell
Department of NanoBiophotonics
Max Planck Institute for Multidisciplinary Sciences
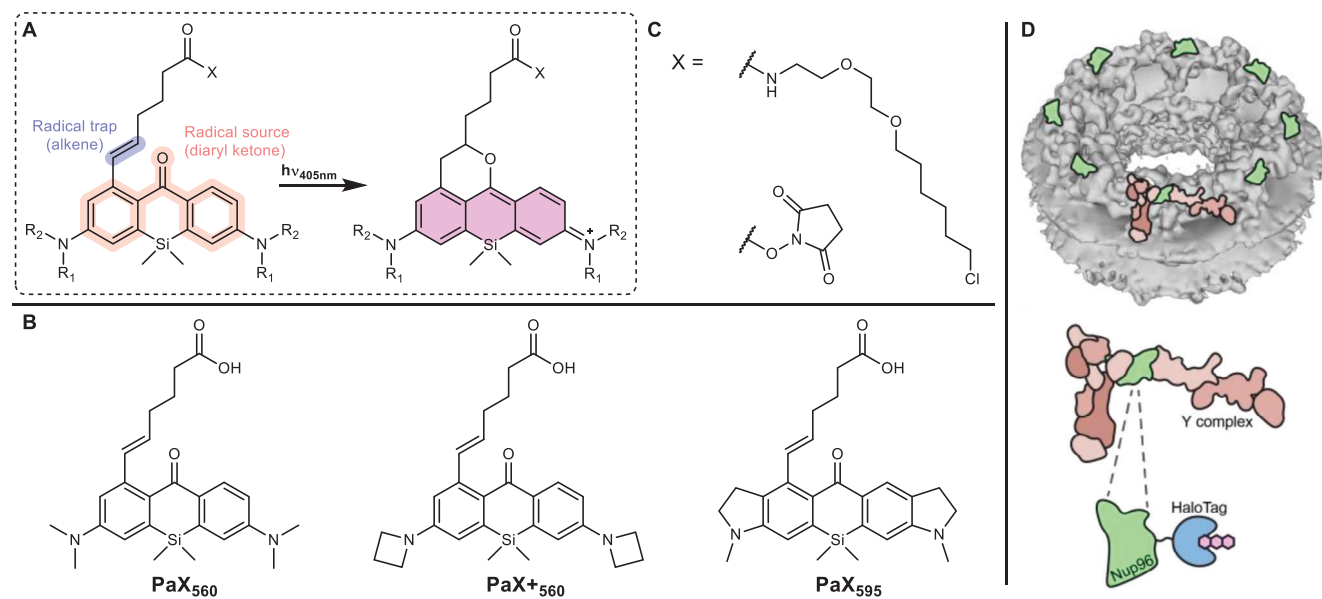37077 Göttingen, Germany

The ORCID identification number(s) for the author(s) of this article can be found under https://doi.org/10.1002/smtd.202301497

[+]Present address: Abberior Instruments America, Bethesda, MD 20814, USA
[++]Present address: Fraunhofer-Institute for Translational Medicine and Pharmacology ITMP, Translational Neuroinflammation and Automated Microscopy TNM, 37073 Göttingen, Germany

1. Introduction

Just like every other optical super-resolution fluorescence microscopy technique, MINimal photon FLUXes (MINFLUX) imaging critically relies on the controlled transition of markers between two distinguishable states.[1–5] Super-resolution concepts relying on the detection and localization of single fluorophores specifically utilize a switch from a non-fluorescent ("off") state to a transiently occupied fluorescent ("on") state and back. By far most of the published MINFLUX imaging data have been acquired with stochastically (on/off) blinking fluorophores, most prominently the cyanine dye Alexa Fluor 647,[6–16] that were extensively optimized for single molecule localization microscopy (SMLM).[4,17–25] While drawing on the fluorophore expertise of the SMLM community enables straightforward acquisition of MINFLUX images, it does not drive the concept to its full potential.

MINFLUX nanoscopy benefits from temporally controlled (nearly deterministic) photoswitching, as it follows the principle of optical coordinate targeting for the localization of individual fluorophores.[5,8,10] More specifically, the zero intensity of a structured excitation beam (e.g., a central minimum of a donut-shaped beam) is actively targeted to the fluorophore of interest (FOI), allowing for the currently most fluorescence-photon-efficient localization by shifting the burden of requiring many photons for localization to the excitation laser and its virtually unlimited supply of photons.[5] As the fluorophores are serially localized with the donut beam, the more temporally deterministic the nature of the implemented molecular switch is, the more efficiently the MINFLUX localization process should run.

The photoswitching mechanism of cyanine dyes is still under investigation, but the most persistent model is based on their photochemical behavior in the presence of thiols and the absence of oxygen.[26] In their triplet state, cyanine dyes can be reduced (via photoinduced electron transfer) by thiolates, followed by a triplet-to-singlet intersystem crossing of the nascent geminate radical pair and radical combination. Cyanine-thiol adduct formation yields the longer-lived "off" state of the dye, while regeneration of the "on" state follows homolytic cleavage and back electron

ADVANCED
SCIENCE NEWS
www.advancedsciencenews.com

small
methods
www.small-methods.com

Scheme 1. Structure of PaX dyes used for 561 nm MINFLUX imaging. A) PaX dyes with their 1-alkenyl radical trap undergo a light-induced assembly into their fluorescent 9-alkoxypyronine photoproduct. B) Structures of PaX$_{560}$, PaX+$_{560}$ and PaX$_{595}$. C) Structure of functional groups used for bioconjugation and HaloTag labeling. D) Schematic representation (electron microscopy (EM) density, EMD-2444) of the NPC (top, grey) and the Y complex (bottom, peach), with the nucleoporin 96 protein (green) fused to HaloTag (blue).

transfer, and can be triggered via indirect illumination (activator/reporter pairs) or via direct illumination with ultraviolet (UV) light (typically 405 nm).[17,18,22,27] However, cyanine photoswitching is still (conditionally) temporally stochastic as (i) the regeneration also happens through a purely thermal (dark) reaction,[27] and as (ii) the excitation wavelength additionally regenerates the "on" state with a non-negligible rate due to spectral broadening of the electronic transition, allowing for SMLM imaging with exclusive irradiation at the absorption maxima of the "on" state.[27–29] Accordingly, the nature of photoswitching of cyanine dyes decreases MINFLUX efficiency by increasing the chance of several markers in the "on" state overlapping in time within a diffraction-determined area. As the excitation intensity zero is guided toward the FOI position by the fluorescent photons of that very same fluorophore, any detection of non-FOI photons will corrupt the localization process. If identified, these localizations are usually discarded, leading to extended measurement times and/or to the loss of information at the respective label position. If not treated separately, these localizations manifest as imaging artifacts at sample positions that do not carry any label.

Due to its truly molecular resolution, MINFLUX nanoscopy gains not only from the completeness of labeling on the sample preparation side but also from a robust and quantitative readout of each label position without a discrepancy between the biochemical labeling efficiency (biological ground truth) and the effective labeling efficiency (image data). In this regard, cyanine dyes in densely labeled samples further impair MINFLUX efficiency by (i) their long-known tendency to form dimers in aqueous solutions at fluorophore distances <2 nm, usually leading to a loss of fluorescence, and by (ii) dipole-dipole induced energy transfer at fluorophore distances <10 nm resulting in accelerated photoswitching.[30–32] In the latter case, the probability of "on" state repopulation is significantly increased by either

fluorescence resonance energy transfer (FRET) from the "on" state (donor) to the "off" state (acceptor) or via additional energy transfer pathways from the trans "on" state to the cis and triplet states.[32–34]

In contrast to stochastically blinking fluorophores, photoactivatable dyes overcome many of these drawbacks by allowing for a more deterministic approach to marker switching. However, applications are often limited by their photolabile protecting groups, reactive byproducts, and non-negligible amounts of misformed (dark) products.[35,36] Recently, a general design strategy for caging-group free photoactivatable fluorescent dyes has been developed by combining a light-responsive 3,6-diaminoxanthone core with an intramolecular alkene radical trap (**Scheme** 1A), which gave rise to a unique class of live-cell compatible functionalized xanthones.[37] Upon one or two-photon irradiation, these photoactivatable xanthone (PaX) dyes assemble efficiently and quantitatively into their respective bright, highly photostable, and nucleophile-resilient dihydropyran-fused pyronine fluorophores. By altering the substitution pattern, the spectral properties as well as the photoactivation rates of the PaX dyes can be reliably controlled. The synthetic route is extendable to carbon- and oxygen-bridged xanthone analogs allowing for spectral tuning across much of the visible spectrum. The versatility and utility of PaX dyes have been demonstrated in multicolor fixed- and live-cell confocal, stimulated emission depletion (STED)[1] and photoactivated localization microscopy (PALM),[4] and a first proof-of-concept application in MINFLUX imaging was reported.[37]

Here, we showcase PaX dyes as potent markers for 561 nm MINFLUX imaging. For a quantitative assessment of their performance, we benchmarked their localization success rate in 2D MINFLUX imaging against the fluorescent protein mMaple, exploiting the nuclear pore complex (NPC) as reference standard.[38,39] PaX$_{560}$ and PaX+$_{560}$ (Scheme 1B) outperformed

ADVANCED
SCIENCE NEWS

www.advancedsciencenews.com

small
methods

www.small-methods.com

the fluorescent protein, establishing them as the first organic dye alternatives to mMaple, currently, the only molecular switch reported for MINFLUX nanoscopy with 561 nm excitation.[8] Rationally designed, the ≈ 35 nm bathochromic shift of the novel PaX$_{595}$ (Scheme 1B) further allowed for dual color 561 nm MINFLUX imaging based on spectral classification. Taking advantage of the deterministic, irreversible, and additive-independent nature of PaX photoactivation, we additionally highlight the dyes' potential for fast live-cell MINFLUX imaging in regular cell medium with PaX$_{560}$.

2. Results

The photo assembly of PaX dyes relies on the co-installation of a radical source (diaryl ketone) and a radical trap (alkene) in close proximity within the xanthone core such that light efficiently triggers the "locking" of the 9-alkoxypyronine fluorophore structure (Scheme 1A).[37] This caging-group free photoactivation mechanism fundamentally differs from the traditional approach of "unlocking" the emissive species by UV-degradation of photolabile caging groups.[35,36,40–48] The current PaX color palette offers two dyes—PaX$_{560}$ and PaX+$_{560}$ (Scheme 1B)—promising to fill the gap in fluorophores dedicated to 561 nm MINFLUX imaging. While both dyes are silicon-bridged xanthone analogs, the additional azetidine groups of PaX+$_{560}$ almost double the dye's brightness ($\Phi_{Fluo} \times \epsilon^{561nm}$, with Φ_{Fluo} being the emission quantum yield and ϵ^{561nm} the absorption coefficient at 561 nm) compared to PaX$_{560}$ (PaX$_{560}$: $\Phi_{Fluo} \times \epsilon^{561nm} = 3.4 \times 10^4$ M^{-1} cm^{-1}, PaX+$_{560}$: $\Phi_{Fluo} \times \epsilon^{561nm} = 6.1 \times 10^4$ M^{-1} cm^{-1}),[37] which can be attributed to the suppression of a non-emissive twisted internal charge transfer state.[49] Interestingly, when we further characterized the relative photostability of PaX$_{560}$ and PaX+$_{560}$ (Figure S1, Supporting Information), we identified that despite the improved brightness of PaX+$_{560}$, the azetidine groups also increased the photobleaching quantum yield. Complementing the photophysical characterization, single molecule traces recorded after photoactivation of PaX$_{560}$ and PaX+$_{560}$ strongly suggest the absence of pronounced transient dark states of the activated dyes (Figure S2, Supporting Information). Any triplet incursions on timescales faster than the MINFLUX temporal resolution are not reflected in our data, even though presumably happening, and consequently leave the data quality of the MINFLUX recordings unaffected. Note that the single-molecule data suggest a certain degree of photoactivation in the absence of activation (405 nm) light (readout activation, Figure S2, Supporting Information).

We additionally reasoned that the introduction of fused indoline auxochromic fragments into the Si-bridged xanthone core should provide a bathochromically shifted PaX dye (similarly to a SiR700 analog of the Si-rhodamine dye[50,51]), complementing PaX$_{560}$ and PaX+$_{560}$ for dual color 561 nm MINFLUX imaging based on spectral classification. Initial density-functional theory (DFT) / time-dependent DFT (TD-DFT) calculations predicted that the indoline fragment would not change the photoactivation behavior/mechanism of the open-form xanthone, compared to PaX$_{560}$ and PaX+$_{560}$ (Figure S3, Supporting Information). Since the previously reported copper-mediated halodeborylation proved to be incompatible with the indoline-bearing ketone, an alternative synthetic sequence was developed to access PaX$_{595}$, involving the oxidative de-borylation with basic hydrogen per-

oxide followed by conversion of the resulting phenol to the aryl triflate (see supporting information for details).[37] The linker incorporating an alkene radical-trap was then installed by Suzuki–Miyaura cross-coupling, yielding PaX$_{595}$ upon deprotection (Scheme 1B). The amino-reactive N-hydroxysuccinimide (NHS) ester derivative (Scheme 1C; Table S1, Supporting Information), the maleimide derivative, and the chloroalkane derivative of the dye were synthesized and characterized (see supporting information for details). PaX$_{595}$ quantitatively converted, upon 405 nm irradiation, into the closed emissive form with an absorption maximum at 595 nm and a fluorescence emission maximum at 630 nm (Figure S4, Supporting Information). Finally, to demonstrate the chemical stability of PaX dyes for live-cell applications, we performed photoactivation assays of PaX$_{560}$, PaX+$_{560}$, and PaX$_{595}$ in lysogeny broth (LB) medium (Figure S5; Table S2, Supporting Information), which provides a mixture of competing biomolecules including amino acids and peptides. We found over 80% of pyronine product formed, even after overnight incubation at 37 °C.

To appraise the performance of PaX dyes in 561 nm MINFLUX imaging, we selected the homozygous knock-in U-2 OS cell line endogenously expressing a fusion construct of nucleoporin Nup96 and HaloTag previously introduced as an in situ reference standard for quantitative super-resolution imaging,[39,52] granting stochiometric tagging (i.e., one HaloTag per target protein) and live-cell compatibility. The stereotypic arrangement of NPC proteins delivers easy-to-analyze reference data for quantifying the microscope performance via molecular counting. As the minimalistic PaX design renders bioconjugation derivatives soluble and cell-membrane permeable, we labeled living cells with chloroalkane PaX derivatives (PaX$_{560}$-Halo, PaX+$_{560}$-Halo, Scheme 1C; Table S1, Supporting Information). To simplify the measurements and make them independent of cell movements, cells were fixed prior to imaging, and the samples were actively stabilized on infrared light back-scattered by the fixed cells. The NPC contains 32 copies of Nup96 – two copies per corner and per cytoplasmic/nucleoplasmic plane – and thus quantitative labeling would provide the option for localizing four fluorophores per corner during 2D imaging (Scheme 1D).[53] Based on the prior knowledge about the eightfold symmetry expected with Nup96 labeling, we sought to investigate the performance of PaX dyes in MINFLUX imaging (Figure S6, Supporting Information) by measuring the average occupancy (Occ), defined as the number of NPC corners containing at least one localization on the Nup96 MINFLUX images (Figure S7, Supporting Information). However, as the observed occupancy depends on both the localization success rate and the actual labeling efficiency, we chose the effective labeling efficiency (ELE) as the figure of merit, a parameter previously established to compare NPC labeling strategies.[39] Note that the actual labeling efficiency itself is a product of various factors including the HaloTag folding efficiency, the substrate cell-permeability, its binding efficiency, and its reactivity. To this end, we implemented an algorithm counting the detected corners of manually identified individual NPCs (Figure S7B, Supporting Information) similar to the approach introduced by Thevathasan et al.[39] and also used by other authors.[54,55]

To use the available photon budget of PaX$_{560}$ and PaX+$_{560}$ most efficiently and guarantee the highest possible localization success rate, we adapted the standard 2D MINFLUX imaging sequence
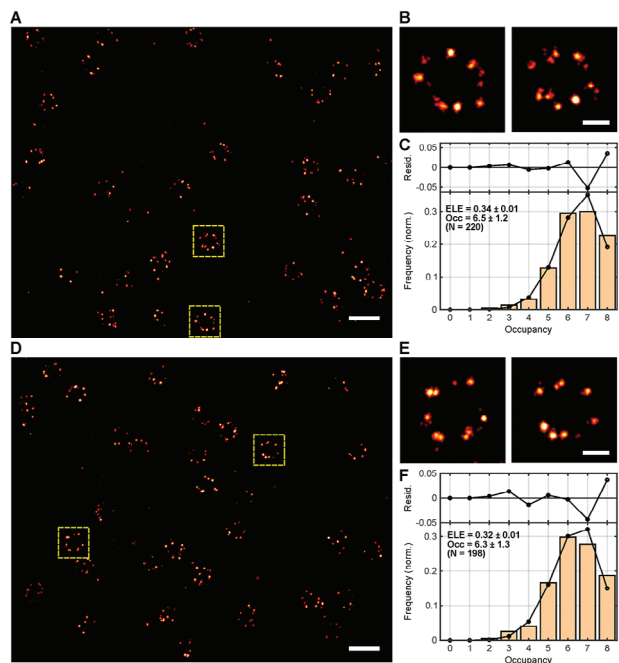
ADVANCED
SCIENCE NEWS

www.advancedsciencenews.com

small
methods

www.small-methods.com

Figure 1. MINFLUX imaging of PaX_{560}- and $PaX+_{560}$-labeled NPCs. Representative MINFLUX images of U-2 OS-CRISPR-NUP96-Halo cells labeled (live) with A,B) PaX_{560}-Halo and D,E) $PaX+_{560}$-Halo, fixed and mounted in phosphate-buffered saline (PBS) prior to imaging; B,E) show zoom-ins of NPCs marked in A and D. Data properties can be found in Figure S6 and Table S4 (Supporting Information). Normalized occupancy histograms of HaloTagged NPCs labeled with C) PaX_{560}-Halo and F) $PaX+_{560}$-Halo. A fit to a probabilistic model is included in each histogram (bars: experimental data, circles: fit), including the residuals in the top plots, considering eight labeling sites and four protein copies at each one (Equation S1, Supporting Information). The fitted ELE value (Figure S9, Supporting Information), the mean occupancy (Occ), and the number of analyzed NPCs (N) are indicated. Scale bars: overviews 200 nm, zoom-ins 50 nm.

provided by the manufacturer to the photophysical properties of the PaX dyes (seq_PaX, Table S3, Supporting Information), achieving a localization precision well under 3 nm with less than 200 photons per localization (PaX_{560}: σ_{xy} = 2.56 nm; $PaX+_{560}$: σ_{xy} = 2.62 nm; **Figure** 1A,B,D,E). Despite the significant difference in the quantum yields measured in cuvette experiments,[37] the total number of detected photons (Table S4, Supporting Information) did not substantially differ between $PaX+_{560}$ and PaX_{560}, accounting for their similar localization precisions. This observation is consistent with the relative photostability of the two fluorophores (Figure S1, Supporting Information). Importantly, we found no significant differences in the mean number of detected NPC corners between the two dyes (PaX_{560}: Occ = 6.5 ± 1.2; $PaX+_{560}$: Occ = 6.3 ± 1.3; Figure 1C,F; Figures S8 and S9, Supporting Information). Remarkably, with an estimated ELE of ≈33%, both PaX dyes grant a similar ELE as reported for other far-red molecular switches commonly used in conventional SMLM, combined with the same labeling strategy (HaloTag), namely Alexa Fluor 647-Halo and Cy5-Halo.[39] Note that these cyanine dyes are typically used in blinking buffers and thus provide several incursions into the "on" state (reportedly 4–26 cycles depending on the dye and the buffer), resulting in multiple opportunities to

localize them successfully.[25,39] Accordingly, the observed PaX ELEs advocate for a high localization success rate of MINFLUX nanoscopy, as the PaX dyes' irreversible switching behavior only grants one opportunity. This, however, offered an alternative approach to assessing the ELE via molecule reassignment to individual emission bursts. We simply counted the number of "on"-events per individual NPC and inferred ELE values slightly larger but comparable to the ones obtained by the Occ analysis (Figure S10, Supporting Information). We attribute the difference primarily to deformations and/or tilting of the individual NPCs but do not rule out the possibility that some "on"-events were incorrectly counted as two. Compared to the ELE of ≈20% reported for the irreversible molecular switch PA-JF549-Halo in SMLM, the significantly greater ELEs of PaX_{560} and $PaX+_{560}$ suggest an improved labeling efficiency to and/or a more quantitative photoactivation than PA-JF549-Halo.[36] Other ELE-compromising factors include early photobleaching and readout activation. To further validate the MINFLUX performance of PaX dyes on target structures other than the NPC, we acquired exemplary 2D MINFLUX data of cytoskeletal filaments. To this end, we labeled living homozygous knock-in U-2 OS cells endogenously expressing a fusion construct of vimentin and HaloTag with PaX_{560}-Halo and fixed the cells prior to 561 nm MINFLUX imaging (Figure S11, Supporting Information).

To establish PaX_{560} and $PaX+_{560}$ as valid alternatives to the photoconvertible protein mMaple for 561 nm MINFLUX imaging, we additionally acquired MINFLUX data of a fusion construct of Nup96 and mMaple endogenously expressed by a second homozygous knock-in U-2 OS reference standard cell line and subjected the data to the same Occ and ELE analysis workflow. In the first step, MINFLUX imaging was performed with the imaging sequence initially optimized for the PaX dyes.[38,39] However, a significant loss of events was noticed ($mMaple_{seq\_PaX}$: Occ = 5.7 ± 1.4, ELE = 27%, **Figure** 2A–C), which may be attributed to the non-negligible probability of transitions into transient dark states (i.e., fast blinking events), the poorer photostability and the approximately three times lower photon budget of mMaple compared to PaX_{560} and $PaX+_{560}$ (Table S4, Supporting Information). Although mMaple offers an arguably higher signaling efficiency than other commonly used irreversibly switching proteins,[56] approximately half of the mMaple population was expected to emit in several microbursts separated by dark times as long as several milliseconds during the "on"-event,[57] as stated in previous reports.[56,58] Despite the more limited photon budget of the fluorescent protein, MINFLUX imaged the mMaple-tagged NPCs with a reasonable localization precision ($mMaple_{seq\_PaX}$: σ_{xy} = 4.92 nm; Figure 2). To allow for the acquisition of the best possible MINFLUX data, an adapted imaging sequence optimized for mMaple was used in the next step to minimize the event loss (seq_mMaple, Table S3, Supporting Information). The most significant difference to seq_PaX was the increase of the localization range (L) from 40 to 100 nm in the last MINFLUX iteration and a more lenient abort criterium on the continuity of the fluorescence photon flux to account for the more complex photophysics. With the adapted sequence, the occupancy and thus the ELE slightly increased ($mMaple_{seq\_mMaple}$: Occ = 5.9 ± 1.2, ELE = 29%, Figure 2D–F), approaching the performance of the PaX dyes. However, seq_mMaple introduced a slight loss of localization precision ($mMaple_{seq\_mMaple}$: σ_{xy} = 5.89 nm;

**ADVANCED
SCIENCE NEWS**

www.advancedsciencenews.com

**small
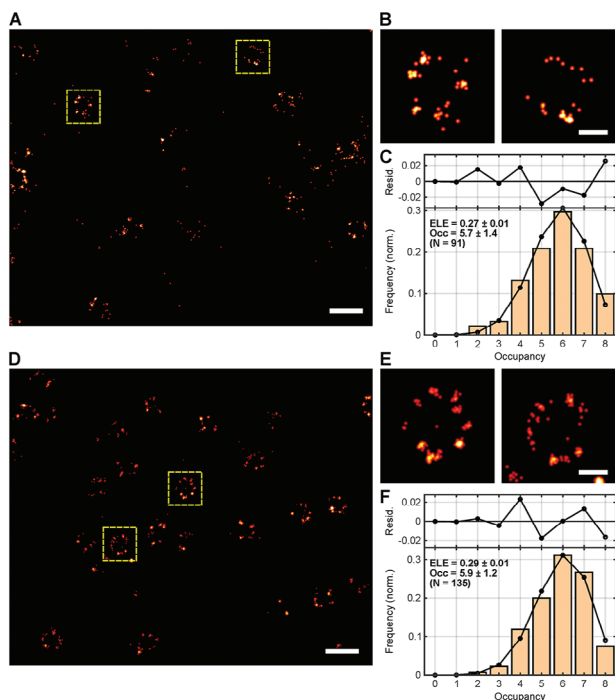methods**

www.small-methods.com

Figure 2. MINFLUX imaging of mMaple-tagged NPCs. Representative MINFLUX images of U-2 OS-CRISPR-NUP96-mMaple, fixed, mounted in 50 mM Tris buffer (pH 8) in 95% D_2O and imaged with A,B) seq_PaX and D,E) seq_mMaple; B,E) show zoom-ins of NPCs marked in A and D. Data properties can be found in Figure S6 and Table S4 (Supporting Information). Normalized occupancy histograms of mMaple-tagged NPCs imaged with C) seq_PaX and with F) seq_mMaple. A fit to a probabilistic model is included in each histogram (bars: experimental data, circles: fit), considering eight labeling sites and four protein copies at each one (Equation S1, Supporting Information). The fitted ELE value (Figure S9, Supporting Information), the mean occupancy (Occ), and the number of analyzed NPCs (N) are indicated. Scale bars: overviews 200 nm, zoom-ins 50 nm.

Figure 2), which can be explained by the 2.5-times larger localization range L in the definitive (last) iteration of that imaging sequence. Compared to the localization precisions, occupancies and *ELE*s achieved with the two PaX dyes, we attribute the generally compromised mMaple performance to its inferiority in brightness (mMaple: $\Phi_{Fluo} \times \epsilon^{561nm} = 1.7 \times 10^4$ $M^{-1}cm^{-1}$), photostability and signaling efficiency,[56] which manifest in a significantly lower number of photons per localization and localizations per "on"-event (Table S4, Supporting Information). Other factors possibly contributing to the discrepancies in MIN-FLUX performance include the protein folding efficiency ($\approx$75% for mMaple,[56] unknown for HaloTag), the mMaple photoconversion efficiency ($\approx$51%[56]), and the mMaple maturation time ($\approx$48 min).[58] Note that the *ELE*s we observed for mMaple significantly differ from the ones found by Thevathasan et al.[39] for SMLM imaging of the fluorescent protein (*ELE* < 30% vs *ELE* = 58%). We assign this discrepancy to the fact that our MINFLUX localization precision allowed for reliably identifying the individual NPC corners, while the SMLM localization precision of Thevathasan et al.[39] did not always grant that. Additionally, the SMLM data suffered more from the more complex photophysics of the fluorescent protein, resulting in a 2.5-fold overcounting

of mMaple copies (i.e., Nup96 copies).[39] Combined, we assume this to translate into an overestimation of mMaple's *ELE* by Thevathasan et al.[39] Interestingly, the *ELE* value we obtained by inferring the number of mMaple copies from individual "on"-events (Figure S10C, Supporting Information) suggests that the longer-lived dark states of the fluorescent protein do not provoke overcounting in MINFLUX as strongly as it does in camera-based localization.

We further exploited the fact that the spectral properties of PaX dyes can be readily tuned by rational design and envisioned PaX_{595} as a potent candidate for complementing PaX_{560} in dual color 561 nm MINFLUX imaging based on spectral classification. While both dyes can be potentially excited at the same wavelength, namely 561 nm (**Figure 3A**), they display a measurable shift in their emission spectra that facilitates the reassignment of the fluorophore type by splitting the single molecule emission into two spectral ranges (580-630 nm and 650–685 nm) detected by two dedicated photon-counting detectors (Figure 3B). To this end, we conjugated secondary antibodies with the aminoreactive NHS ester PaX_{595} derivative (Scheme 1C; Table S1, Supporting Information) and indirectly immunolabeled against nucleoporin Nup62 after live-labeling Nup96-Halo with PaX_{560}-Halo (Scheme 1C; Table S1, Supporting Information) in the respective homozygous knock-in U-2 OS cell line.[39] While all molecule position estimates were calculated using the photons detected with both detectors (PaX_{560}/PaX_{595}: $\sigma_{xy} = 1.75$ nm), the fraction of photon counts for each spectral detection window (detector channel ratio, *DCR*) (Figure 3C; Figure S12, Supporting Information) allowed for fluorophore classification in the rendered MINFLUX image (Figure 3D; Figures S13 and S14; Table S5, Supporting Information for data properties). Estimations of the theoretical DCR values (Figure S12, Supporting Information) show the correct tendency but are not accurate due to the unknown shape of the filters used in the microscope for channel separation, and probably due to small variations in the emission spectra in response to a different microenvironment. The PaX_{560} localizations representing Nup96 appeared in the stereotypic NPC arrangement as expected, whereas the PaX_{595} localizations representing Nup62, a component of the central transport channel, accumulated in the center of the NPC ring. Comparing the allegedly observed and spectrally expected fluorophore miss-classification (Figure S15, Supporting Information), we assign the presence of misplaced localizations (i.e., localizations conflicting with the known NPC positions of the target proteins) mainly to non-specific staining, specifically for the PaX_{595} immunofluorescence labeling strategy against Nup62 (i.e., off-target binding of the primary and/or the secondary antibodies). This result qualifies PaX_{595} as a useful partner to PaX_{560} for dual color, single 561 nm excitation MINFLUX imaging, based on spectral classification.[53]

Finally, to fully explore all the advantages of PaX dyes, we assessed the possibility of live-cell MINFLUX imaging with PaX_{560}, exploiting its irreversible switching behavior. It must be noted that actively stabilizing the sample on the infrared light backscattered by living cells was not possible due to their movement. Moreover, the introduction of gold beads as fiducial markers was not well-tolerated by the cells, probably due to the cytotoxic effects of the bead's capping and/or stabilizing agents. Thus, to avoid being strongly affected by (sub)cellular dynamics and
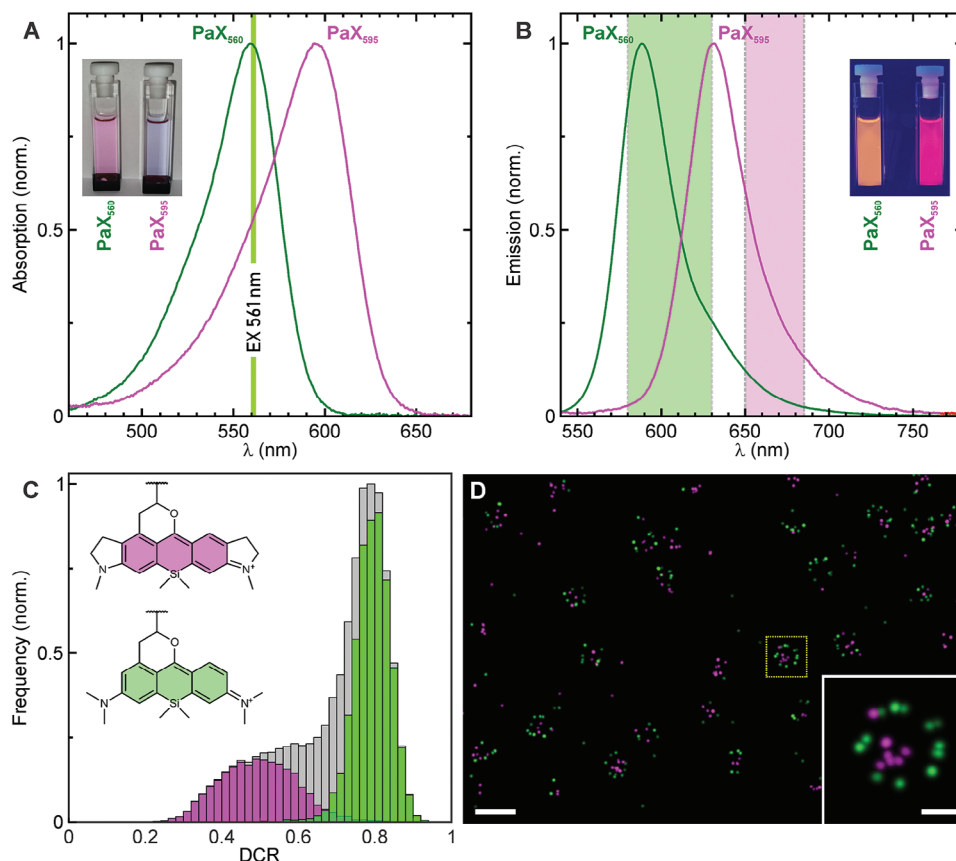
Figure 3. Dual color 561 nm MINFLUX imaging with PaX$_{560}$ and PaX$_{595}$ based on spectral classification. A) Absorption and B) emission spectra of solutions of PaX$_{560}$ and PaX$_{595}$ in methanol after complete activation with 405 nm light. The excitation wavelength (561 nm) and the detection windows used for MINFLUX imaging are indicated in the corresponding plots. The inset shows the color of the solutions under A) normal and B) UV (366 nm) illumination. C) Histogram of the DCR value of all localizations (grey) and the ones after spectral classification (green/magenta). D) Dual color MINFLUX image of NPCs in fixed U-2 OS-CRISPR-NUP96-Halo cells labeled with PaX$_{560}$-Halo (Nup96, green), and with a primary antibody against Nup62 (magenta) in combination with a secondary antibody conjugated with PaX$_{595}$. The inset shows a selected NPC. The spectral decomposition of the image is shown in Figure S13 (Supporting Information). Data properties can be found in Figure S14 and Table S5 (Supporting Information). Scale bars: overview 200 nm, zoom-in 50 nm.

potential sample drift during the measurement, we minimized the acquisition time by imaging small regions of interest (ROI < 500 nm×500 nm) that typically contained one or two NPCs (**Figure 4**; Figures S16 and S17, Supporting Information), and increased the activation power to maximize the measurement efficiency. Despite the lack of active sample stabilization, NPCs of living cells were successfully imaged in 60–120 s with a remarkable localization precision < 3 nm (Table S6, Supporting Information). We assign the difference in the NPC appearance to the fixed-cell data to a combination of cellular motion, motion of the NPC itself,[54,59] and a certain flexibility of the HaloTag relative to Nup96. In general, the NPC population of a cell is marked by a pronounced heterogeneity and variability in terms of NPC symmetry, diameter, ellipticity, and twist angle between the cytoplasmic and nucleoplasmic planes, with individual NPCs strongly deviating from the idealized picture of a perfectly symmetrical ring suggested by structure averaging approaches.[60] Processed the same way as the dual color fixed-cell data (Table S6, Supporting Information), the PaX$_{560}$ live-cell data feature almost twice the localizations per event (PaX$_{560}$ live versus fixed: *Locs/Event* = 20 vs 13) and a similar number of photons per localization (PaX$_{560}$ live

vs fixed: *Photons/Loc* = 110 vs 121). Although this leads to significantly more detected photons per event (PaX$_{560}$ live vs fixed: *Photons/Event* = 2220 vs 1572), the live-cell MINFLUX localization precision is slightly compromised (PaX$_{560}$ live vs fixed: σ_{xy} = 2.81 vs 1.73 nm). Consequently, we attribute the small loss of precision to the missing active sample stabilization, and minor (sub)cellular movements during the live-cell MINFLUX measurements.

3. Discussion

MINFLUX pioneers a novel concept of super-resolution based on switching single molecules, that shifts the main photon burden from the emission of the fluorophores to their absorption and at the same time provides each fluorescence photon with more information content than in conventional localization. Thus, fluorophore design can prioritize other dye characteristics such as molecule compactness, live-cell permeability and compatibility, and the nature of the molecular switch, as it just recently has been showcased with the introduction of the novel class of PaX dyes.[37] Like all photoactivatable fluorophores, they offer only a
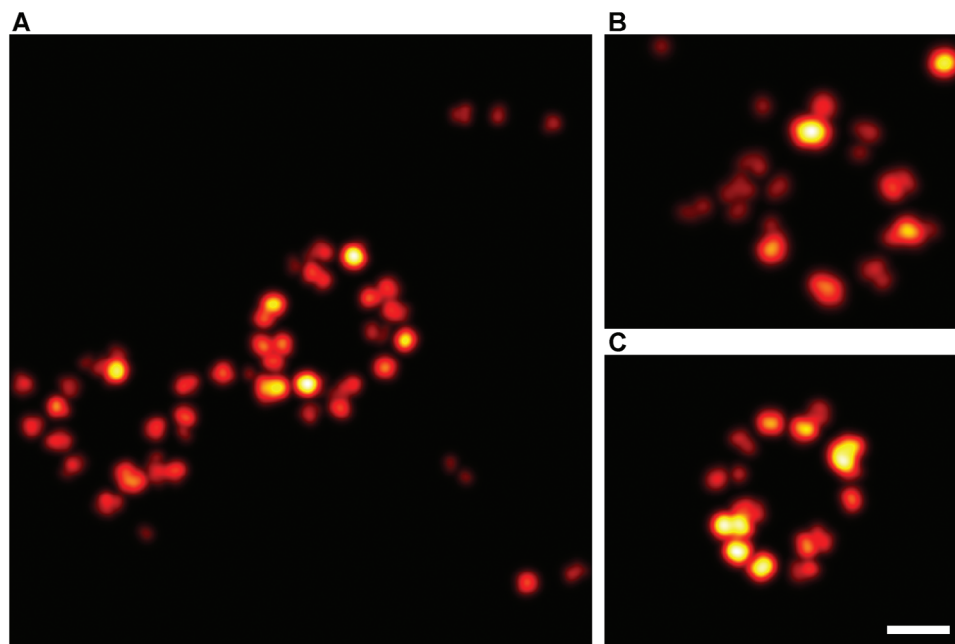
Figure 4. Live-cell MINFLUX imaging of PaX$_{560}$-labeled NPCs. Representative MINFLUX images of living U-2 OS-CRISPR-NUP96-Halo cells labeled with compound PaX$_{560}$-Halo and imaged in complete cell medium without any special additives. Total imaging times were A) 120, B) 50, and C) 80 s. The image generation over time of A is shown in Figure S16 (Supporting Information). Data properties can be found in Figure S17 and Table S6 (Supporting Information). Scale bar: 50 nm.

single emission burst after deterministic "on"-switching. Their irreversible photoswitching nature provides the advantage of preventing multiple redundant localization attempts of the same molecule, which not only renders the data acquisition highly efficient but also pushes the imaging speed for smaller ROIs beyond the time scale of (slower) (sub)cellular movement, allowing for the acquisition of live-cell MINFLUX data. Moreover, it facilitates quantitative data analysis by allowing for molecule reassignment to individual emission bursts and thus for molecular counting. When combined with quantitative labeling such as endogenous tagging, the potential for molecular identification and protein quantification can be fully exploited.

The downside to irreversible photoswitching is having only one opportunity to successfully localize the markers. Thus, maximizing the localization success rate is of utmost importance to MINFLUX imaging, especially with photoactivatable fluorophores, as it is for any imaging strategy relying on single molecule detection. To quantitatively assess and benchmark the MINFLUX performance of PaX dyes, we based the direct comparison of PaX$_{560}$ and PaX+$_{560}$ with the fluorescent protein mMaple on the readily measurable *ELE*, relying on the endogenous labeling and imaging of a specific NPC protein (Nup96) as a reference standard.[38,39] We observed no significant differences in the *ELE* between the two investigated PaX dyes, and a superior MINFLUX performance of PaX$_{560}$ and PaX+$_{560}$ over mMaple, one of the best irreversibly switching fluorescent proteins in the given spectral range.[38,58] In addition, the *ELE*s obtained with PaX$_{560}$ and PaX+$_{560}$ are comparable to the best *ELE*s obtained with established blinking cyanine dyes (Alexa Fluor 647 and Cy5) and outperform the *ELE* of state-of-the-art photoactivatable live-cell

dyes (PA-JF549) using the same labeling strategy and a SMLM setup.[39]

While mMaple had previously proven to be suitable for 561 nm MINFLUX imaging, measurements had to be conducted in 95% deuterium oxide with 5% Tris buffer to suppress excursions into transient dark states and increase the photon budget, even with living cells.[8,61] In contrast, PaX$_{560}$-Halo equally enabled NPC labeling on the endogenous level, but additionally allowed for the acquisition of live-cell MINFLUX data in a complete cell medium, eliminating any stress on the cells introduced by bioincompatible buffers and/or photostabilizing additives. Although mMaple's irreversible photoswitching behavior theoretically qualifies for molecular counting, its transient dark times are expected to lead to an overcounting error[62] and its tendency to dimerize can influence the target protein distribution.[58] Together with mMaple's poorer photostability and lower photon budget as compared to PaX$_{560}$ and PaX+$_{560}$, and its non-quantitative folding, maturation, and photoconversion, MINFLUX data acquisition must compromise on localization precision and success rate.[38,58]

To this end, PaX$_{560}$ and PaX+$_{560}$ promise to be a valid alternative, as they are compatible with many live-cell labeling and imaging strategies.[37] These PaX dyes grant high *ELE*s by combining efficient HaloTag labeling and an uncompromised localization success rate for MINFLUX imaging. Rational design not only brought about the bathochromically shifted PaX$_{595}$, which enabled dual color 561 nm MINFLUX imaging based on spectral classification, but also promises the development of other PaX representatives suitable for 640 nm MINFLUX imaging and for pseudocolor multiplexing by selective photoactivation. Just as

the development of MINFLUX is driving the design and development of novel molecular switches with dedicated properties, we expect PaX dyes to likewise boost applications in fluorescence nanoscopy and the development of HaloTag-based biosensors.[63]

4. Experimental Section

A detailed description of the materials and experimental methods, including dye synthesis, sample preparation, MINFLUX setup description, data acquisition, and data analysis are provided in the Supporting Information.

Supporting Information

Supporting Information is available from the Wiley Online Library or from the author.

Conflict of Interest

R.L., A.N.B., and M.L.B. are inventors on patent application no. WO 2023/284968 A1 filed by the Max Planck Society that covers the photoactivatable fluorescent dyes of this work and their use. S.W.H. is a co-founder and J.M. is an employee of the company Abberior Instruments America, which commercializes super-resolution microscopy systems, including MINFLUX. S.W.H. holds patent rights on the principles, embodiments, and procedures of MINFLUX. The other authors declare no conflict of interest.

Author Contributions

M.R. performed labeling and MINFLUX microscopy. M.R., M.L.B., J.M., and J.K.-F. performed data analysis. R.L. was responsible for the PaX concept. R.L. and A.N.B. performed the chemical synthesis. M.L.B. and R.L. performed dye characterization. J.M. and M.L.B. conceived the study. J.M. wrote the manuscript with input from R.L. and M.L.B. S.W.H. and J.M. directed and supervised the investigations. S.W.H. developed MINFLUX nanoscopy and proposed the development of MINFLUX-specific fluorophores. All authors discussed the results and commented on the manuscript.

Data Availability Statement

The data that support the findings of this study are available from the corresponding author upon reasonable request.

[1] S. W. Hell, J. Wichmann, *Opt. Lett.* **1994**, *19*, 780.
[2] T. A. Klar, S. Jakobs, M. Dyba, A. Egner, S. W. Hell, *Proc. Natl. Acad. Sci. USA* **2000**, *97*, 8206.
[3] M. J. Rust, M. Bates, X. Zhuang, *Nat. Methods* **2006**, *3*, 793.
[4] E. Betzig, G. H. Patterson, R. Sougrat, O. W. Lindwasser, S. Olenych, J. S. Bonifacino, M. W. Davidson, J. Lippincott-Schwartz, H. F. Hess, *Science* **2006**, *313*, 1642.
[5] F. Balzarotti, Y. Eilers, K. C. Gwosch, A. H. Gynna, V. Westphal, F. D. Stefani, J. Elf, S. W. Hell, *Science* **2017**, *355*, 606.
[6] T. Stephan, C. Bruser, M. Deckers, A. M. Steyer, F. Balzarotti, M. Barbot, T. S. Behr, G. Heim, W. Hubner, P. Ilgen, F. Lange, D. Pacheu-Grau, J. K. Pape, S. Stoldt, T. Huser, S. W. Hell, W. Mobius, P. Rehling, D. Riedel, S. Jakobs, *EMBO J.* **2020**, *39*, 104105.
[7] J. K. Pape, T. Stephan, F. Balzarotti, R. Buchner, F. Lange, D. Riedel, S. Jakobs, S. W. Hell, *Proc. Natl. Acad. Sci. USA* **2020**, *117*, 20607.
[8] K. C. Gwosch, J. K. Pape, F. Balzarotti, P. Hoess, J. Ellenberg, J. Ries, S. W. Hell, *Nat. Methods* **2020**, *17*, 217.
[9] L. A. Masullo, F. Steiner, J. Zahringer, L. F. Lopez, J. Bohlen, L. Richter, F. Cole, P. Tinnefeld, F. D. Stefani, *Nano Lett.* **2021**, *21*, 840.
[10] R. Schmidt, T. Weihs, C. A. Wurm, I. Jansen, J. Rehman, S. J. Sahl, S. W. Hell, *Nat. Commun.* **2021**, *12*, 1478.
[11] A. Carsten, M. Rudolph, T. Weihs, R. Schmidt, I. Jansen, C. A. Wurm, A. Diepold, A. V. Failla, M. Wolters, M. Aepfelbacher, *Methods Appl. Fluoresc.* **2022**, *11*, 015004.
[12] C. P. Grabner, I. Jansen, J. Neef, T. Weihs, R. Schmidt, D. Riedel, C. A. Wurm, T. Moser, *Sci. Adv.* **2022**, *8*, eabl7560.
[13] M. Hara, M. Ariyoshi, T. Sano, R. S. Nozawa, S. Shinkai, S. Onami, I. Jansen, T. Hirota, T. Fukagawa, *Mol. Cell* **2023**, *83*, 2188.
[14] V. Jackson, J. Hermann, C. J. Tynan, D. J. Rolfe, R. A. Corey, A. L. Duncan, M. Noriega, A. Chu, A. C. Kalli, E. Y. Jones, M. S. P. Sansom, M. L. Martin-Fernandez, E. Seiradake, M. Chavent, *Structure* **2022**, *30*, 1354.
[15] A. H. Clowsley, A. Meletiou, E. Lučinskaitė, I. Jansen, P. P. Jones, W. E. Louch, C. Soeller, *bioRxiv* **2023**, 550636.
[16] E. M. Mulhall, A. Gharpure, R. M. Lee, A. E. Dubin, J. S. Aaron, K. L. Marshall, K. R. Spencer, M. A. Reiche, S. C. Henderson, T. L. Chew, A. Patapoutian, *Nature* **2023**, *620*, 1117.
[17] M. Heilemann, E. Margeat, R. Kasper, M. Sauer, P. Tinnefeld, *J. Am. Chem. Soc.* **2005**, *127*, 3801.
[18] M. Bates, T. R. Blosser, X. Zhuang, *Phys. Rev. Lett.* **2005**, *94*, 108101.
[19] H. Bock, C. Geisler, C. A. Wurm, C. Von Middendorff, S. Jakobs, A. Schönle, A. Egner, S. W. Hell, C. Eggeling, *Appl. Phys. B-Lasers and Optics* **2007**, *88*, 161.
[20] M. Bates, B. Huang, G. T. Dempsey, X. Zhuang, *Science* **2007**, *317*, 1749.
[21] B. Huang, W. Wang, M. Bates, X. Zhuang, *Science* **2008**, *319*, 810.
[22] M. Heilemann, S. van de Linde, M. Schuttpelz, R. Kasper, B. Seefeldt, A. Mukherjee, P. Tinnefeld, M. Sauer, *Angew. Chem. Int. Ed. Engl.* **2008**, *47*, 6172.
[23] M. Bates, B. Huang, X. Zhuang, *Curr. Opin. Chem. Biol.* **2008**, *12*, 505.
[24] M. Heilemann, S. van de Linde, A. Mukherjee, M. Sauer, *Angew. Chem. Int. Ed. Engl.* **2009**, *48*, 6903.

ADVANCED
SCIENCE NEWS

www.advancedsciencenews.com

small
methods

www.small-methods.com

[25] G. T. Dempsey, J. C. Vaughan, K. H. Chen, M. Bates, X. Zhuang, *Nat. Methods* **2011**, *8*, 1027.

[26] A. Lisovskaya, I. Carmichael, A. Harriman, *J. Phys. Chem. A* **2021**, *125*, 5779.

[27] Y. Gidi, L. Payne, V. Glembockyte, M. S. Michie, M. J. Schnermann, G. Cosa, *J. Am. Chem. Soc.* **2020**, *142*, 12681.

[28] M. Sauer, M. Heilemann, *Chem. Rev.* **2017**, *117*, 7478.

[29] J. Cnossen, T. Hinsdale, R. O. Thorsen, M. Siemons, F. Schueder, R. Jungmann, C. S. Smith, B. Rieger, S. Stallinga, *Nat. Methods* **2020**, *17*, 59.

[30] J. L. Bricks, Y. L. Slominskii, I. D. Panas, A. P. Demchenko, *Methods Appl. Fluoresc.* **2017**, *6*, 012001.

[31] E. S. Emerson, M. A. Conlin, A. E. Rosenoff, K. S. Norland, H. Rodriguez, D. Chin, G. R. Bird, *J. Phys. Chem.* **2002**, *71*, 2396.

[32] D. A. Helmerich, G. Beliu, D. Taban, M. Meub, M. Streit, A. Kuhlemann, S. Doose, M. Sauer, *Nat. Methods* **2022**, *19*, 986.

[33] T. Förster, *Ann. Phys.* **1948**, *437*, 55.

[34] G. D. Scholes, *Annu. Rev. Phys. Chem.* **2003**, *54*, 57.

[35] V. N. Belov, C. A. Wurm, V. P. Boyarskiy, S. Jakobs, S. W. Hell, *Angew. Chem. Int. Ed. Engl.* **2010**, *49*, 3520.

[36] J. B. Grimm, B. P. English, H. Choi, A. K. Muthusamy, B. P. Mehl, P. Dong, T. A. Brown, J. Lippincott-Schwartz, Z. Liu, T. Lionnet, L. D. Lavis, *Nat. Methods* **2016**, *13*, 985.

[37] R. Lincoln, M. L. Bossi, M. Remmel, E. D'Este, A. N. Butkevich, S. W. Hell, *Nat. Chem.* **2022**, *14*, 1013.

[38] A. L. McEvoy, H. Hoi, M. Bates, E. Platonova, P. J. Cranfill, M. A. Baird, M. W. Davidson, H. Ewers, J. Liphardt, R. E. Campbell, *PLoS One* **2012**, *7*, e51314.

[39] J. V. Thevathasan, M. Kahnwald, K. Cieslinski, P. Hoess, S. K. Peneti, M. Reitberger, D. Heid, K. C. Kasuba, S. J. Hoerner, Y. Li, Y. L. Wu, M. Mund, U. Matti, P. M. Pereira, R. Henriques, B. Nijmeijer, M. Kueblbeck, V. J. Sabinina, J. Ellenberg, J. Ries, *Nat. Methods* **2019**, *16*, 1045.

[40] J. Folling, V. Belov, R. Kunetsky, R. Medda, A. Schonle, A. Egner, C. Eggeling, M. Bossi, S. W. Hell, *Angew. Chem. Int. Ed. Engl.* **2007**, *46*, 6266.

[41] L. M. Wysocki, J. B. Grimm, A. N. Tkachuk, T. A. Brown, E. Betzig, L. D. Lavis, *Angew. Chem. Int. Ed. Engl.* **2011**, *50*, 11206.

[42] V. N. Belov, M. L. Bossi, J. Folling, V. P. Boyarskiy, S. W. Hell, *Chemistry (Easton)* **2009**, *15*, 10762.

[43] D. Puliti, D. Warther, C. Orange, A. Specht, M. Goeldner, *Bioorg. Med. Chem.* **2011**, *19*, 1023.

[44] S. Banala, D. Maurel, S. Manley, K. Johnsson, *ACS Chem. Biol.* **2012**, *7*, 289.

[45] V. N. Belov, G. Y. Mitronova, M. L. Bossi, V. P. Boyarskiy, E. Hebisch, C. Geisler, K. Kolmakov, C. A. Wurm, K. I. Willig, S. W. Hell, *Chemistry (Easton)* **2014**, *20*, 13162.

[46] J. B. Grimm, T. Klein, B. G. Kopek, G. Shtengel, H. F. Hess, M. Sauer, L. D. Lavis, *Angew. Chem. Int. Ed. Engl.* **2016**, *55*, 1723.

[47] M. Weber, T. A. Khan, L. J. Patalag, M. Bossi, M. Leutenegger, V. N. Belov, S. W. Hell, *Chemistry (Easton)* **2021**, *27*, 451.

[48] A. N. Butkevich, M. Weber, A. R. Cereceda Delgado, L. M. Ostersehlt, E. D'Este, S. W. Hell, *J. Am. Chem. Soc.* **2021**, *143*, 18388.

[49] J. B. Grimm, B. P. English, J. Chen, J. P. Slaughter, Z. Zhang, A. Revyakin, R. Patel, J. J. Macklin, D. Normanno, R. H. Singer, T. Lionnet, L. D. Lavis, *Nat. Methods* **2015**, *12*, 244.

[50] Y. Koide, Y. Urano, K. Hanaoka, W. Piao, M. Kusakabe, N. Saito, T. Terai, T. Okabe, T. Nagano, *J. Am. Chem. Soc.* **2012**, *134*, 5029.

[51] G. Lukinavicius, L. Reymond, K. Umezawa, O. Sallin, E. D'Este, F. Gottfert, H. Ta, S. W. Hell, Y. Urano, K. Johnsson, *J. Am. Chem. Soc.* **2016**, *138*, 9365.

[52] G. V. Los, L. P. Encell, M. G. McDougall, D. D. Hartzell, N. Karassina, C. Zimprich, M. G. Wood, R. Learish, R. F. Ohana, M. Urh, D. Simpson, J. Mendez, K. Zimmerman, P. Otto, G. Vidugiris, J. Zhu, A. Darzins, D. H. Klaubert, R. F. Bulleit, K. V. Wood, *ACS Chem. Biol.* **2008**, *3*, 373.

[53] A. Szymborska, A. de Marco, N. Daigle, V. C. Cordes, J. A. Briggs, J. Ellenberg, *Science* **2013**, *341*, 655.

[54] R. Chowdhury, A. Sau, S. M. Musser, *Nat. Cell Biol.* **2022**, *24*, 112.

[55] M. Weber, H. von der Emde, M. Leutenegger, P. Gunkel, S. Sambandan, T. A. Khan, J. Keller-Findeisen, V. C. Cordes, S. W. Hell, *Nat. Biotechnol.* **2023**, *41*, 569.

[56] N. Durisic, L. Laparra-Cuervo, A. Sandoval-Alvarez, J. S. Borbely, M. Lakadamyali, *Nat. Methods* **2014**, *11*, 156.

[57] M. Byrdin, C. Duan, D. Bourgeois, K. Brettel, *J. Am. Chem. Soc.* **2018**, *140*, 2897.

[58] S. Wang, J. R. Moffitt, G. T. Dempsey, X. S. Xie, X. Zhuang, *Proc. Natl. Acad. Sci. USA* **2014**, *111*, 8452.

[59] F. Y. Chu, S. C. Haley, A. Zidovska, *Proc. Natl. Acad. Sci. USA* **2017**, *114*, 10338.

[60] M. Theiss, J. K. Heriche, C. Russell, D. Helekal, A. Soppitt, J. Ries, J. Ellenberg, A. Brazma, V. Uhlmann, *Bioinformatics* **2023**, *39*.

[61] W. Q. Ong, Y. R. Citron, J. Schnitzbauer, D. Kamiyama, B. Huang, *Chem. Commun. (Camb.)* **2015**, *51*, 13451.

[62] S. H. Lee, J. Y. Shin, A. Lee, C. Bustamante, *Proc. Natl. Acad. Sci. USA* **2012**, *109*, 17436.

[63] A. Cook, F. Walterspiel, C. Deo, *ChemBioChem* **2023**, *24*, 202300022.